

Wall-modeled large-eddy simulation based on building-block flows

By Y. Ling[†], G. Arranz[†], E. Williams[†], K. Goc, K. Griffin AND A. Lozano-Durán[†]

A unified subgrid-scale (SGS) and wall model for large-eddy simulation (LES) is proposed by devising the flow as a collection of building blocks that enables the prediction of the eddy viscosity. The core assumption of the model is that simple canonical flows contain the essential physics to provide accurate predictions of the SGS tensor in more complex flows. The model is constructed to predict zero-pressure-gradient wall-bounded turbulence, adverse pressure gradient effects, separation and laminar flow. The approach is implemented using a Bayesian classifier, which identifies the contribution of each building block in the flow, and a neural-network-based predictor, which estimates the eddy viscosity based on the building-block units. The training data are directly obtained from wall-modeled LES with an exact SGS/wall model for the mean quantities to guarantee consistency with the numerical discretization. The model is validated in canonical flows and the NASA High-Lift Common Research Model and shown to improve the predictions with respect to current modeling approaches.

1. Introduction

The ability to accurately simulate complex flows using computational fluid dynamics (CFD) is crucial in many applications ranging from aircraft design to drag reduction in pipelines (Smits & Marusic 2013). In recent years, wall-modeled large-eddy simulation (WMLES) has gained traction as an alternative to traditional lower-fidelity models, such as Reynolds-averaged Navier-Stokes (RANS)-based methods. Compared to RANS-based methods, WMLES is inherently unsteady and better positioned to provide high accuracy in the presence of non-equilibrium flows such as separation. Additionally, since WMLES only resolves the large-scale motions far from the wall, its computational cost is competitive compared to other CFD approaches (Choi & Moin 2012; Yang & Griffin 2021). Recently, Goc *et al.* (2021) have shown that WMLES is close to achieving the accuracy and turnaround times demanded by the aerospace industry. While state-of-the-art WMLES performs satisfactorily in turbulent boundary layers with sufficient grid resolution, its performance deteriorates in the presence of less than 20 grid points per boundary layer thickness. Unfortunately, the latter grid resolution is typical for external aerodynamics applications (Lozano-Durán *et al.* 2022). In this report, we present a unified SGS/wall model consistent with the numerical discretization and applicable to complex geometries. The model is rooted in the idea that truly revolutionary improvements in WMLES will encompass advancements in numerics, grid generation and wall/SGS modeling.

The model is implemented using artificial neural networks (ANNs) within the supervised learning paradigm, which has been extensively explored for modeling in recent years. For example, SGS models have been trained using data from filtered direct numerical simulation (DNS) (Gamahara & Hattori 2017; Xie *et al.* 2019). Examples of

[†] Department of Aeronautics and Astronautics, Massachusetts Institute of Technology

supervised learning for wall modeling include Yang *et al.* (2019), Zhou *et al.* (2021), Zangeneh (2021) and Huang *et al.* (2019), to name a few. Interestingly, most studies to date have trained the model with data from higher-fidelity simulations, such as DNS or wall-resolved LES. As a consequence, previous models ignored the nonnegligible errors arising from the numerical discretization in actual WMLES. An exception is the work by Bae & Koumoutsakos (2022) using reinforcement learning. Here, we take advantage of a novel data preparation process to ensure numerical consistency between the training data and the model deployed in the flow solver.

The report is organized as follows. Section 2 details the simulation setup, numerical approach, model formulation, control scheme and training procedure. Results for different test cases are presented in Section 3. These include laminar channel flow, turbulent channel flow, turbulent Poiseuille-Couette flow and the NASA High-Lift Common Research Model (CRM-HL). Finally, concluding remarks are offered in Section 4.

2. Methodology

2.1. Model overview

The model presented is based on the hypothesis that complex flows can be divided into subregions resembling canonical building-block flows. Following the strategy proposed by Lozano-Durán & Bae (2020), we devise a model composed of a classifier and a predictor. The classifier categorizes the flow into different types of canonical flows, and the predictor provides the wall stress and eddy viscosity based on the likelihood of each category. The model is referred to as the BFM (building-block flow model). In this work, we consider four types of building-block flows, viz., laminar channel flow, fully developed turbulent channel flow, turbulent Poiseuille-Couette flow with adverse pressure gradient and turbulent Poiseuille-Couette flow with “separation”.

The model architecture is summarized in Figure 1. The model inputs are the invariants of rate-of-strain and rate-of-rotation tensors (\bar{S}_{ij} and \bar{R}_{ij} , respectively), which are defined as

$$\begin{aligned} I_1 &= \text{tr}(\bar{\mathbf{S}}^2), & I_2 &= \text{tr}(\bar{\mathbf{R}}^2), \\ I_3 &= \text{tr}(\bar{\mathbf{S}}^3), & I_4 &= \text{tr}(\bar{\mathbf{S}}\bar{\mathbf{R}}^2), \\ I_5 &= \text{tr}(\bar{\mathbf{S}}^2\bar{\mathbf{R}}^2), & I_6 &= \text{tr}(\bar{\mathbf{S}}^2\bar{\mathbf{R}}^2\bar{\mathbf{S}}\bar{\mathbf{R}}), \end{aligned} \quad (2.1)$$

where \bar{S}_{ij} and \bar{R}_{ij} are

$$\bar{S}_{ij} = \frac{1}{2} \begin{pmatrix} \partial\bar{u}_i & \partial\bar{u}_j \\ \partial x_j & \partial x_i \end{pmatrix}, \quad \bar{R}_{ij} = \frac{1}{2} \begin{pmatrix} \partial\bar{u}_i & \partial\bar{u}_j \\ \partial x_j & -\partial x_i \end{pmatrix}. \quad (2.2)$$

The anisotropic component of the resolved shear stress is given by the eddy-viscosity model

$$\bar{\tau}_{ij}^d = -2\nu_t\bar{S}_{ij}, \quad (2.3)$$

and the eddy viscosity is assumed to be a function of the invariants (Lund & Novikov 1993)

$$\nu_t = f(I_1, I_2, I_3, I_4, I_5, I_6, \theta), \quad (2.4)$$

where f represents an ANN, and θ denotes additional input variables, namely, ν , Δ and u_{\parallel} , where ν is the kinematic viscosity, $\Delta = \sqrt{\Delta x^2 + \Delta y^2 + \Delta z^2}$ is the characteristic grid size and u_{\parallel} is the magnitude of the wall-parallel velocity measured with respect to the wall. The latter is only used for the ANN close to the wall. The mapping between inputs

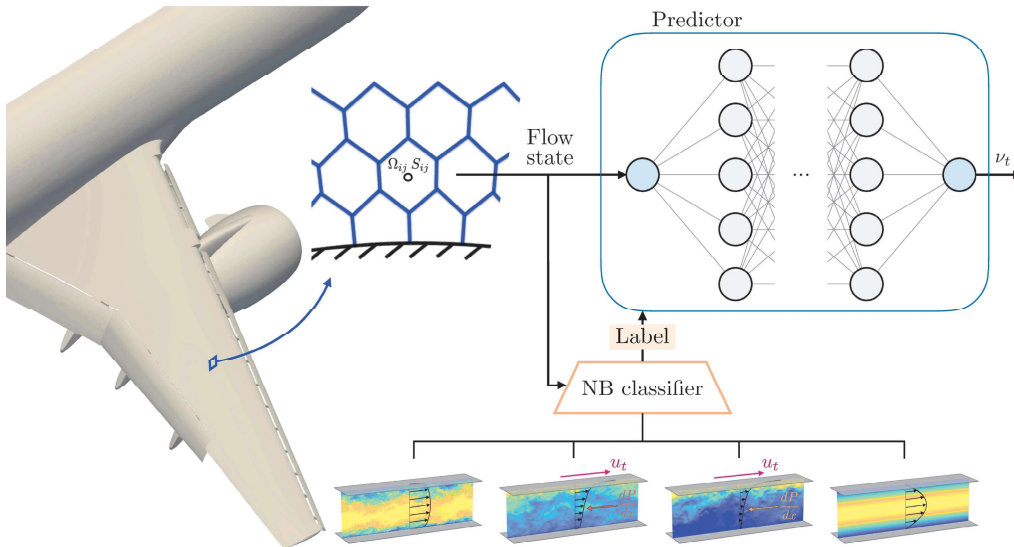


FIGURE 1. Schematic of the building-block flow model. The panel shows the classifier-predictor structure and the ANN architecture. The flow state refers to $(I_1, \dots, I_6, \nu, \Delta, u_{\parallel})$ and different ANNs are used for the inner and outer layer. The bottom of the figure depicts the building-block flows considered (from left to right): turbulent channel flow, Poiseuille-Couette flow with mild adverse pressure gradient, Poiseuille-Couette flow with separation and laminar Poiseuille flow.

and output is learned from data generated from controlled WMLES simulations, which are detailed in Section 2.2.

The input and output variables of the ANN are given in nondimensional form. This is crucial for the generalizability of the model. The nondimensionalization of the input and output features is done using parameters that are local in both time and space to guarantee the applicability of the model to complex geometries. Two types of ANNs are considered. For grid points at the wall and the first grid points off the wall, the input and output quantities are nondimensionalized using viscous scaling (ν and Δ). For the rest of the points, the input and output variables are nondimensionalized using semi-viscous scaling $[(\sqrt{2\bar{S}_{ij}}\bar{S}_{ij}\nu)^{1/2}$ and $\Delta]$.

The simulations for canonical cases are performed using the solver by Bae & Lozano-Durán (2021) (i.e., the incompressible, staggered, second-order accurate central finite difference method). The CRM-HL simulation is carried out in charLES, a finite-volume, compressible flow solver. Readers are referred to Goc *et al.* (2021) for more details about charLES.

2.2. Building blocks and data preparation

Figure 1 also illustrates the collection of building-block flows. The Poiseuille flow is used to generally represent laminar flows. The turbulent channel flow models the regime where turbulence is fully developed without significant mean-pressure gradient effects. In both cases, the bottom and top walls are static. In the turbulent Poiseuille-Couette flows, the top wall moves at a constant speed (u_t) in the streamwise direction, and an adverse pressure gradient is applied in the direction opposed to the top wall velocity. The adverse

pressure gradient ranges from mild to strong, so that the flow separates (i.e., zero wall stress) on the bottom wall.

The training data is generated using WMLES with an exact-for-the-mean eddy-viscosity and wall model (denoted by ESGS). This enables the model to account for the numerical errors of the flow solver. The ESGS model is based on the anisotropic minimum-dissipation (AMD) SGS model (Rozema *et al.* 2015) combined with a controller that iteratively adjusts the AMD eddy viscosity to match the DNS mean velocity profile. A Dirichlet non-slip boundary condition is applied at the walls and the correct wall-shear stress is enforced by augmenting the eddy viscosity at the walls such that $\nu_t|_w = (\partial\bar{u}/\partial y)|_w^{-1} \tau_w/\rho - \nu$, following Bae & Lozano-Durán (2021). For turbulent channel flows, the mean DNS quantities are obtained from the database by Jimenez and coworkers (Del Alamo *et al.* 2004; Hoyas & Jiménez 2006; Lozano-Durán & Jiménez 2014). Four cases with friction Reynolds numbers 550, 950, 2000 and 4200 are used. For the turbulent Poiseuille-Couette flows, our in-house code is used to generate DNS data. Two cases (labeled as PC-0 and PC-2) are considered, which correspond to separation and adverse pressure gradient, respectively. The Reynolds numbers based on the adverse pressure gradient are $Re_P = \sqrt{h^3 dP/dx}/\nu = 680$ and 340 , and the Reynolds number based on the top wall velocity is $Re_U = u_t h/\nu = 22,360$. The computational domain is $L_x \times L_y \times L_z = 4\pi h \times 2h \times 2\pi h$ for channel flows and $L_x \times L_y \times L_z = 2\pi h \times 2h \times \pi h$ for PC-0 and PC-2, where h is the channel half-height. The grid size for the WMLES cases with ESGS is $\Delta \approx 0.2h$.

2.3. Predictor and classifier

The architecture of the ANNs is a fully connected feedforward neural network with 6 hidden layers and 40 neurons per layer. The model comprises different ANNs. The first ANN is used to predict the eddy viscosity far from the wall, where viscous effects are negligible (i.e., outer layer ANN). To account for near-wall viscous effects, two ANNs are used to predict ν_t at the wall and at the first grid point off the wall. The input features to the outer layer ANN are $(I_1, \dots, I_6, \nu, \Delta)$. For inner layer ANNs, the input features are identical to the outer layer ANN in addition to $u_{||}$. The ANNs were trained using stochastic gradient descent by randomly dividing training data into two groups, the training set (80% of the data) and test set (20% of the data). For laminar flows, the eddy viscosity is set to zero.

The classification of the flow at a given point is done in two steps. First, the flow is classified as turbulent or laminar. If the flow is turbulent, it is further classified as zero-pressure-gradient wall turbulence (ZPG), adverse-pressure-gradient wall turbulence (APG), or separated turbulent flow. A Naive Bayes (NB) classifier is employed whose inputs are the nondimensionalized invariants (together with $u_{||}$ normalized with ν/Δ for the second classification). For the turbulent/laminar classifier, the invariants are normalized with ν and Δ , whereas for the second classification, $\sqrt{2\bar{S}_{ij}\bar{S}_{ij}}$ is used. The output of the classifier is a label that is fed to the predictor, as shown in Figure 1.

The classifier is trained with the same cases as the predictor in addition to synthetic data generated for laminar Poiseuille flow at $Re_\tau = [5 - 150]$. The classifier is applied to all grid points to discern between turbulent and laminar flow. The second classification is only applied to the points in contact with the wall. The classifier shows 100% accuracy in the first classification. For the turbulent classification, Figure 2(a) shows the confusion matrix. The numbers in the cells indicate the percentage of samples that are classified as a given class, showing that flows are predicted with $> 75\%$ accuracy.

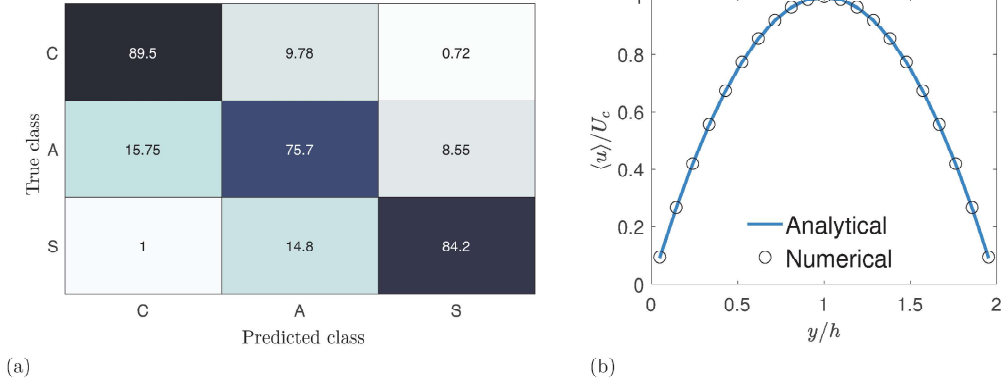


FIGURE 2. (a) Confusion matrix of the classifier for the first grid point off wall. C stands for ZPG flow, A for APG flow and S for separated flow. (b) Mean streamwise velocity profile for laminar channel flow (U_c is the centerline velocity).

3. Results

3.1. Laminar channel flow

The BFM is first tested in a laminar channel flow with fixed centerline velocity. The simulation is started from a random flow field and the data are collected after transients. As shown in Figure 2(b), the BFM produces the same solution as the analytical one by correctly classifying all the points as laminar flow. Regarding wall-shear stress, the analytical solution corresponds to a friction Reynolds number $Re_\tau = 19.64$, and the prediction of BFM is $Re_\tau = 19.62$.

3.2. Turbulent channel flow

The BFM is next tested in turbulent channel flows. Two grid sizes ($\Delta = 0.2h$ and $\Delta = 0.1h$) are considered to assess the generalizability of the model. The results of BFM are compared with the Dynamic Smagorinsky (DSM) and Vreman SGS models using the ODE-based equilibrium wall model (EQWM) by Larsson *et al.* (2016). The mean velocity profiles are shown in Figure 3, and Table 1 summarizes the friction Reynolds number predicted by WMLES. BFM exhibits the best performance in the coarse grid. The predictions of BFM deteriorate when the grid size is refined as shown in Figure 4; however, they are still comparable to those from traditional models. In this preliminary version of BFM, the model was trained only at one grid resolution. Better grid-convergence behavior is expected in future versions of BFM trained at various grid sizes.

3.3. Turbulent Poiseuille-Couette flow

Three cases are considered: PC0 (separation), PC1 (stronger APG) and PC2 (mild APG). The mean velocity profiles and wall-shear stress predictions are shown in Figure 5 and Table 1, respectively. As shown in Table 1, BFM gives the best wall-stress predictions for all cases. For PC0, BFM is capable of capturing separation better than other models. For PC2 and PC1, the improvement is marginal. As shown in Figure 5, BFM also outperforms or matches the accuracy of other models in terms of the prediction of the mean velocity profile except for PC1. The classifier was found to be responsible for hindering the overall performance in this case. Assuming a perfect classification for PC1, the results by BFM

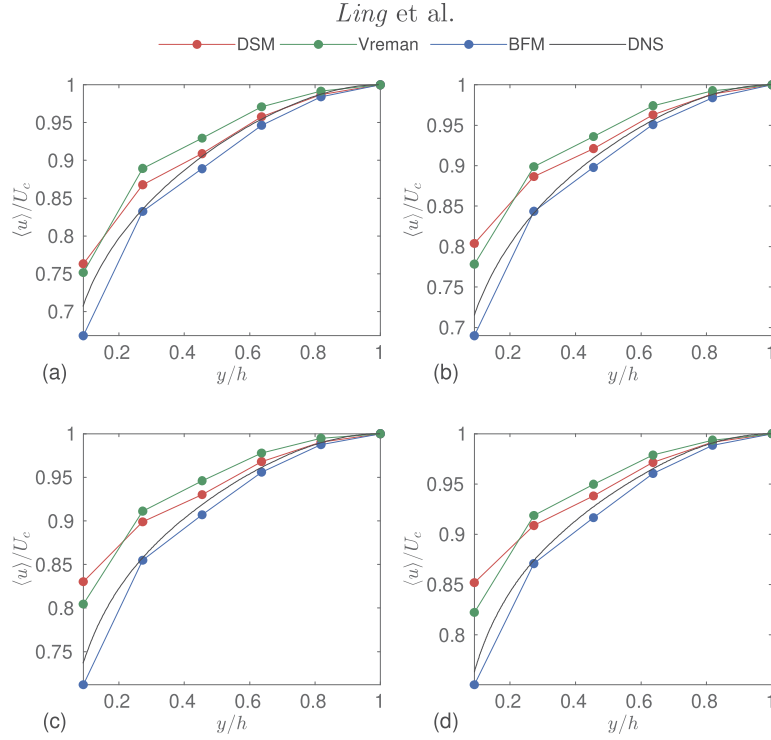


FIGURE 3. Mean streamwise velocity for turbulent channel flow using a coarse grid ($\Delta = 0.2h$). (a) $Re_\tau \approx 550$, (b) $Re_\tau \approx 950$, (c) $Re_\tau \approx 2000$ and (d) $Re_\tau \approx 4200$.

Case	Re_τ	DSM-EQWM	Vreman-EQWM	BFM	Trained	Re_P
550-C	547	587(7.3%)	578(5.7%)	540(1.3%)	✓	N/A
950-C	943	1034(9.7%)	1002(6.3%)	929(1.5%)	✓	N/A
2000-C	2003	2228(11.2%)	2157(7.7%)	1976(1.3%)	✓	N/A
4200-C	4179	4641(11.1%)	4474(7.1%)	4179(0.0%)	✓	N/A
550-M	547	552(0.9%)	545(0.4%)	537(1.8%)	×	N/A
950-M	943	973(3.2%)	944(0.1%)	906(3.9%)	×	N/A
2000-M	2003	2137(6.7%)	2050(2.3%)	1988(0.7%)	×	N/A
4200-M	4179	4502(7.7%)	4286(2.6%)	4006(4.1%)	×	N/A
PC0	7	76(1014%)	68(871%)	33(371%)	✓	680
PC1	194	164(15.5%)	169(12.9%)	172(11.3%)	×	480
PC2	264	225(14.8%)	221(16.3%)	227(14.0%)	✓	340

TABLE 1. Friction Reynolds numbers predicted by different SGS and wall models. Re_τ are the benchmark values from DNS. The “Trained” column shows whether the case has been used for training. Cases ended with M were simulated with a finer grid ($\Delta = 0.1h$). Numbers in parentheses are the relative errors defined by $|(Re_{\tau, \text{pred}} - Re_\tau)/Re_\tau|$. Re_P is the Reynolds number defined by the adverse pressure gradient applied.

outperform other models, as shown in Figure 5. A more accurate classifier is anticipated to help the model achieve better mean profile and wall-shear stress predictions.

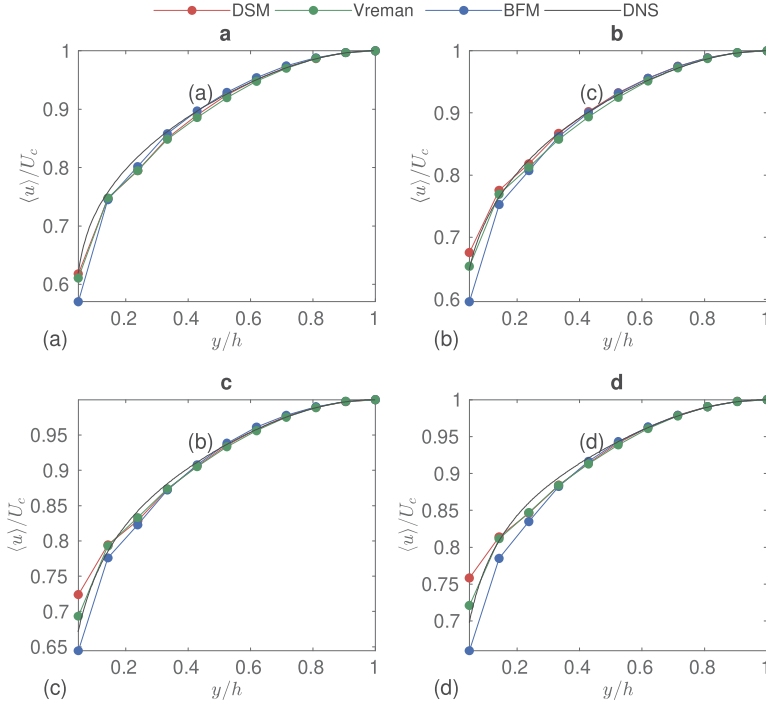


FIGURE 4. Mean streamwise velocity for turbulent channel flow using a medium grid ($\Delta = 0.1h$). (a) $Re_\tau \approx 550$, (b) $Re_\tau \approx 950$, (c) $Re_\tau \approx 2000$ and (d) $Re_\tau \approx 4200$.

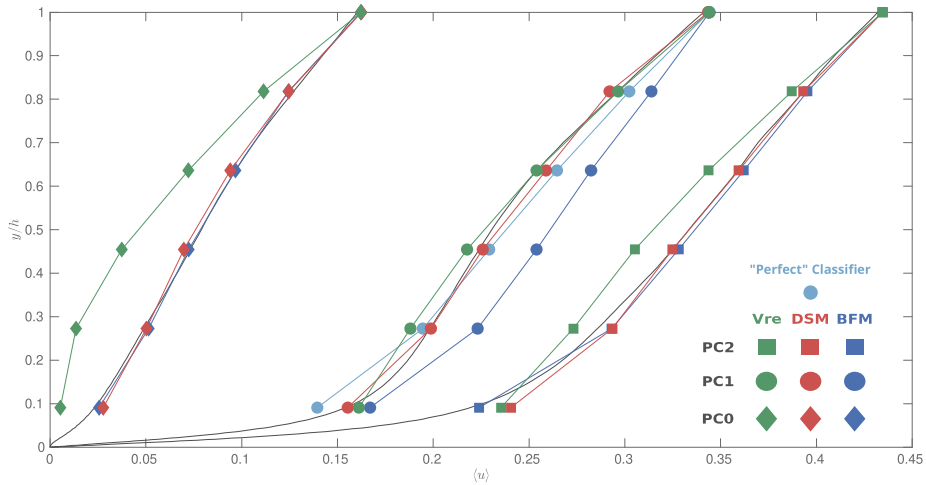


FIGURE 5. Mean streamwise velocity for Poiseuille-Couette flow. Three cases, PC0 (separation), PC1 (stronger APG) and PC2 (mild APG), are overlaid on the same plots.

3.4. CRM-HL

Finally, BFM is tested in the CRM-HL as representative of realistic aircraft in high-lift configuration (Lacy & Sclafani 2016). We focus on free air simulations. The reader is referred to Goc *et al.* (2022) for a detailed description of the physical and numerical setup.

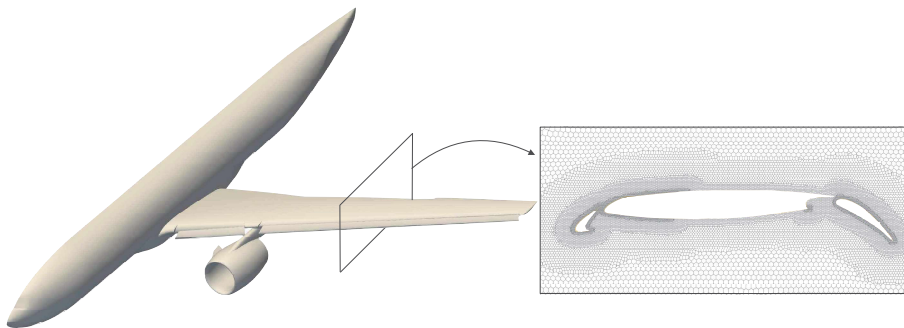


FIGURE 6. Geometry of the CRM-HL model and a cross-sectional view of the grid over the wing surface.

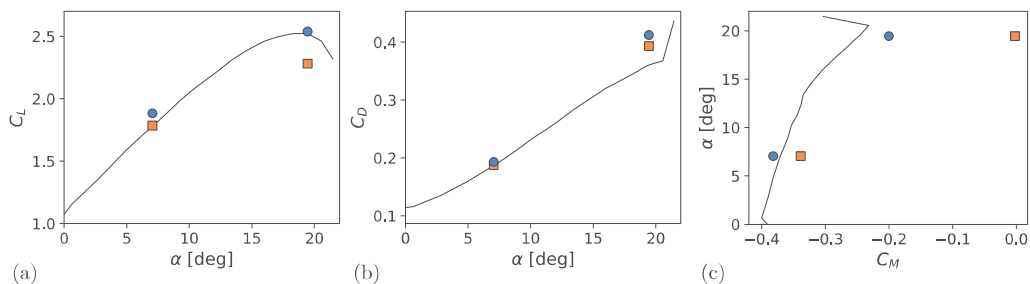


FIGURE 7. (a) Lift, (b) drag and (c) pitching moment coefficients for CRM-HL. The black lines denote experimental results, squares are for DSM-EQWM and circles are for BFM.

We perform simulations for two angles of attack, $\alpha = 7.05^\circ$ and 19.57° , and compare the lift, drag and pitching moment coefficients with experimental data and simulations from Goc *et al.* (2022) using DSM with EQWM (labeled as DSM-EQWM). The grid has 40 million elements and is the same as in Goc *et al.* (2022). A slice of the grid is depicted in Figure 6. The simulations are conducted in charLES with a version of BFM that assumes ZPG. Future versions of BFM will be retrained using WMLES data from charLES to guarantee accuracy in the classification and consistency with the numerical discretization.

Figure 7 displays the lift, drag and pitching moment coefficients. For $\alpha = 7.05^\circ$, DSM-EQWM correctly predicts C_L and C_D . However, further analysis has shown that this accurate prediction is coincidental and due to error cancellation when integrating the total forces. This is corroborated by the poor predictions of pitching moment by DSM-EQWM. However, BFM provides more consistent results. The case of $\alpha = 19.57^\circ$ corresponds to the angle of attack of maximum lift coefficient. DSM-EQWM underpredicts the C_L , whereas BFM accurately predicts C_L . The drag coefficient is overpredicted by both models, but the pitching moment computed using BFM is closer to the experimental values, suggesting that BFM provides a more accurate distribution of the forces over the wing. Inspection of the sectional pressure coefficient (Figure 8) indicates that BFM maintains the flow attached over a longer section of the wing compared to DSM-EQWM, which explains the enhanced performance of BFM.

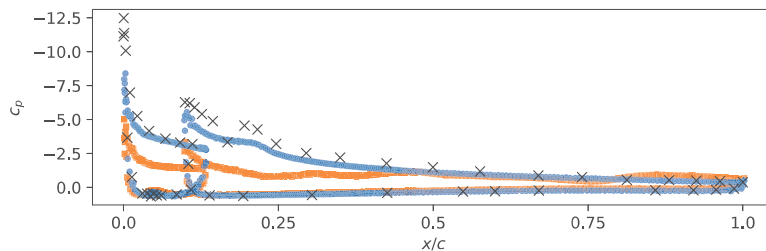


FIGURE 8. Pressure coefficient at the 82% spanwise section of the wing for $\alpha = 19.57^\circ$. Black \times represents experimental results, orange squares are for DSM-EQWM and blue circles are for BFM.

4. Conclusions

We have presented a unified SGS/wall model for large-eddy simulation by devising the flow as a collection of building blocks whose information enables the prediction of the SGS stress tensor. The model is referred to as the building-block flow model (BFM) and is grounded in the idea that truly revolutionary improvements in WMLES will encompass advancements in machine-learning-based modeling consistent with the numerics and grid generation.

The first version of BFM discussed here is constructed to predict wall-attached turbulence, adverse-pressure-gradient turbulence, separation and laminar flow. The model is trained using WMLES with an exact-for-the-mean SGS/wall model that guarantees consistency with the numerical schemes and the gridding strategy. The model is applicable to complex geometries and is implemented using artificial neural networks.

The BFM has been validated in canonical flows. These include laminar Poiseuille flow, turbulent channel flows, and turbulent Poiseuille-Couette flows mimicking adverse-pressure-gradient effects and separation. The performance of BFM in complex scenarios is evaluated in the NASA Common Research Model High-Lift (CRM-HL). We have shown that BFM outperforms traditional SGS/wall models in the canonical flows and the CRM-HL. The only exceptions are the coincidentally accurate predictions by the equilibrium wall model due to error cancellation. To the best of our knowledge, this is the first demonstration of a successful SGS/wall model implemented via artificial neural networks applicable to realistic aircraft configurations.

Acknowledgments

The authors acknowledge the MIT SuperCloud and Lincoln Laboratory Supercomputing Center for providing HPC resources that have contributed to the research results reported within this paper.

REFERENCES

- BAE, H. J. & KOUMOUTSAKOS, P. 2022 Scientific multi-agent reinforcement learning for wall-models of turbulent flows. *Nat. Commun.* **13**, 1443.
- BAE, H. J. & LOZANO-DURÁN, A. 2021 Effect of wall boundary conditions on a wall-modeled large-eddy simulation in a finite-difference framework. *Fluids* **6**, 112.
- CHOI, H. & MOIN, P. 2012 Grid-point requirements for large eddy simulation: Chapman estimates revisited. *Phys. Fluids* **24**, 011702.

- DEL ALAMO, J. C., JIMÉNEZ, J., ZANDONADE, P. & MOSER, R. D. 2004 Scaling of the energy spectra of turbulent channels. *J. Fluid Mech.* **500**, 135–144.
- GAMAHARA, M. & HATTORI, Y. 2017 Searching for turbulence models by artificial neural network. *Phys. Rev. Fluids* **2**, 054604.
- GOC, K., BOSE, S. T. & MOIN, P. 2022 Large eddy simulation of the NASA high-lift common research model. In *AIAA SCITECH 2022 Forum*, p. 1556.
- GOC, K. A., LEHMKUHL, O., PARK, G. I., BOSE, S. T. & MOIN, P. 2021 Large eddy simulation of aircraft at affordable cost: a milestone in computational fluid dynamics. *Flow* **1**, E14.
- HOYAS, S. & JIMÉNEZ, J. 2006 Scaling of the velocity fluctuations in turbulent channels up to $Re_\tau = 2003$. *Phys. Fluids* **18** (1), 011702.
- HUANG, X. L., YANG, X. I. & KUNZ, R. F. 2019 Wall-modeled large-eddy simulations of spanwise rotating turbulent channels—Comparing a physics-based approach and a data-based approach. *Phys. Fluids* **31**, 125105.
- LACY, D. S. & SCLAFANI, A. J. 2016 Development of the high lift common research model (hl-crm): A representative high lift configuration for transonic transports. In *54th AIAA Aerospace Sciences Meeting*, p. 308.
- LARSSON, J., KAWAI, S., BODART, J. & BERMEJO-MORENO, I. 2016 Large eddy simulation with modeled wall-stress: recent progress and future directions. *Mech. Eng. Rev.* **3**, 15–00418.
- LOZANO-DURÁN, A. & BAE, H. J. 2020 Self-critical machine-learning wall-modeled LES for external aerodynamics. *Annual Research Briefs*, Center for Turbulence Research, Stanford University, pp. 197–210.
- LOZANO-DURÁN, A., BOSE, S. T. & MOIN, P. 2022 Performance of wall-modeled LES with boundary-layer-conforming grids for external aerodynamics. *AIAA J.* **60**, 747–766.
- LOZANO-DURÁN, A. & JIMÉNEZ, J. 2014 Effect of the computational domain on direct simulations of turbulent channels up to $Re_\tau = 4200$. *Phys. Fluids* **26**, 011702.
- LUND, T. S. & NOVIKOV, E. 1993 Parameterization of subgrid-scale stress by the velocity gradient tensor. *Annual Research Briefs*, Center for Turbulence Research, Stanford University, pp. 27–43.
- ROZEMA, W., BAE, H. J., MOIN, P. & VERSTAPPEN, R. 2015 Minimum-dissipation models for large-eddy simulation. *Phys. Fluids* **27**, 085107.
- SMITS, A. J. & MARUSIC, I. 2013 Wall-bounded turbulence. *Phys. Today* **66**, 25–30.
- XIE, C., WANG, J., LI, H., WAN, M. & CHEN, S. 2019 Artificial neural network mixed model for large eddy simulation of compressible isotropic turbulence. *Phys. Fluids* **31**, 085112.
- YANG, X. I. A. & GRIFFIN, K. P. 2021 Grid-point and time-step requirements for direct numerical simulation and large-eddy simulation. *Phys. Fluids* **33**, 015108.
- YANG, X. I. A., ZAFAR, S., WANG, J.-X. & XIAO, H. 2019 Predictive large-eddy-simulation wall modeling via physics-informed neural networks. *Phys. Rev. Fluids* **4**, 034602.
- ZANGENEH, R. 2021 Data-driven model for improving wall-modeled large-eddy simulation of supersonic turbulent flows with separation. *Phys. Fluids* **33**, 126103.
- ZHOU, Z., HE, G. & YANG, X. 2021 Wall model based on neural networks for LES of turbulent flows over periodic hills. *Phys. Rev. Fluids* **6**, 054610.

supervised learning for wall modeling include Yang *et al.* (2019), Zhou *et al.* (2021), Zangeneh (2021) and Huang *et al.* (2019), to name a few. Interestingly, most studies to date have trained the model with data from higher-fidelity simulations, such as DNS or wall-resolved LES. As a consequence, previous models ignored the nonnegligible errors arising from the numerical discretization in actual WMLES. An exception is the work by Bae & Koumoutsakos (2022) using reinforcement learning. Here, we take advantage of a novel data preparation process to ensure numerical consistency between the training data and the model deployed in the flow solver.

The report is organized as follows. Section 2 details the simulation setup, numerical approach, model formulation, control scheme and training procedure. Results for different test cases are presented in Section 3. These include laminar channel flow, turbulent channel flow, turbulent Poiseuille-Couette flow and the NASA High-Lift Common Research Model (CRM-HL). Finally, concluding remarks are offered in Section 4.

2. Methodology

2.1. Model overview

The model presented is based on the hypothesis that complex flows can be divided into subregions resembling canonical building-block flows. Following the strategy proposed by Lozano-Durán & Bae (2020), we devise a model composed of a classifier and a predictor. The classifier categorizes the flow into different types of canonical flows, and the predictor provides the wall stress and eddy viscosity based on the likelihood of each category. The model is referred to as the BFM (building-block flow model). In this work, we consider four types of building-block flows, viz., laminar channel flow, fully developed turbulent channel flow, turbulent Poiseuille-Couette flow with adverse pressure gradient and turbulent Poiseuille-Couette flow with “separation”.

The model architecture is summarized in Figure 1. The model inputs are the invariants of rate-of-strain and rate-of-rotation tensors (\bar{S}_{ij} and \bar{R}_{ij} , respectively), which are defined as

$$\begin{aligned} I_1 &= \text{tr}(\bar{\mathbf{S}}^2), & I_2 &= \text{tr}(\bar{\mathbf{R}}^2), \\ I_3 &= \text{tr}(\bar{\mathbf{S}}^3), & I_4 &= \text{tr}(\bar{\mathbf{S}}\bar{\mathbf{R}}^2), \\ I_5 &= \text{tr}(\bar{\mathbf{S}}^2\bar{\mathbf{R}}^2), & I_6 &= \text{tr}(\bar{\mathbf{S}}^2\bar{\mathbf{R}}^2\bar{\mathbf{S}}\bar{\mathbf{R}}), \end{aligned} \quad (2.1)$$

where \bar{S}_{ij} and \bar{R}_{ij} are

$$\bar{S}_{ij} = \frac{1}{2} \left(\frac{\partial \bar{u}_i}{\partial x_j} + \frac{\partial \bar{u}_j}{\partial x_i} \right), \quad \bar{R}_{ij} = \frac{1}{2} \left(\frac{\partial \bar{u}_i}{\partial x_j} - \frac{\partial \bar{u}_j}{\partial x_i} \right). \quad (2.2)$$

The anisotropic component of the resolved shear stress is given by the eddy-viscosity model

$$\bar{\tau}_{ij}^d = -2\nu_t \bar{S}_{ij}, \quad (2.3)$$

and the eddy viscosity is assumed to be a function of the invariants (Lund & Novikov 1993)

$$\nu_t = f(I_1, I_2, I_3, I_4, I_5, I_6, \theta), \quad (2.4)$$

where f represents an ANN, and θ denotes additional input variables, namely, ν , Δ and u_{\parallel} , where ν is the kinematic viscosity, $\Delta = \sqrt{\Delta x^2 + \Delta y^2 + \Delta z^2}$ is the characteristic grid size and u_{\parallel} is the magnitude of the wall-parallel velocity measured with respect to the wall. The latter is only used for the ANN close to the wall. The mapping between inputs

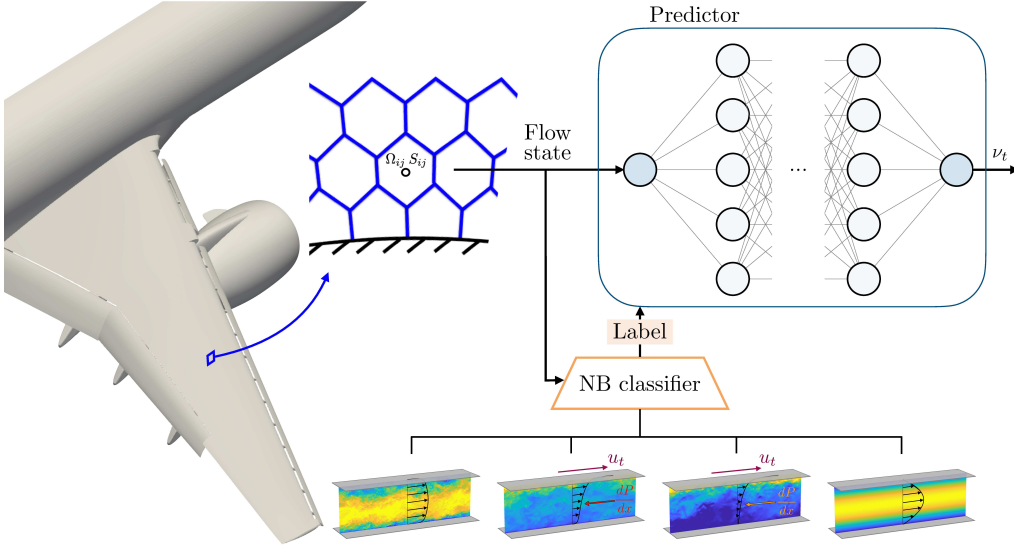


FIGURE 1. Schematic of the building-block flow model. The panel shows the classifier-predictor structure and the ANN architecture. The flow state refers to $(I_1, \dots, I_6, \nu, \Delta, u_{||})$ and different ANNs are used for the inner and outer layer. The bottom of the figure depicts the building-block flows considered (from left to right): turbulent channel flow, Poiseuille-Couette flow with mild adverse pressure gradient, Poiseuille-Couette flow with separation and laminar Poiseuille flow.

and output is learned from data generated from controlled WMLES simulations, which are detailed in Section 2.2.

The input and output variables of the ANN are given in nondimensional form. This is crucial for the generalizability of the model. The nondimensionalization of the input and output features is done using parameters that are local in both time and space to guarantee the applicability of the model to complex geometries. Two types of ANNs are considered. For grid points at the wall and the first grid points off the wall, the input and output quantities are nondimensionalized using viscous scaling (ν and Δ). For the rest of the points, the input and output variables are nondimensionalized using semi-viscous scaling $[(\sqrt{2S_{ij}S_{ij}}\nu)^{1/2}$ and $\Delta]$.

The simulations for canonical cases are performed using the solver by Bae & Lozano-Durán (2021) (i.e., the incompressible, staggered, second-order accurate central finite difference method). The CRM-HL simulation is carried out in charLES, a finite-volume, compressible flow solver. Readers are referred to Goc *et al.* (2021) for more details about charLES.

2.2. Building blocks and data preparation

Figure 1 also illustrates the collection of building-block flows. The Poiseuille flow is used to generally represent laminar flows. The turbulent channel flow models the regime where turbulence is fully developed without significant mean-pressure gradient effects. In both cases, the bottom and top walls are static. In the turbulent Poiseuille-Couette flows, the top wall moves at a constant speed (u_t) in the streamwise direction, and an adverse pressure gradient is applied in the direction opposed to the top wall velocity. The adverse

pressure gradient ranges from mild to strong, so that the flow separates (i.e., zero wall stress) on the bottom wall.

The training data is generated using WMLES with an exact-for-the-mean eddy-viscosity and wall model (denoted by ESGS). This enables the model to account for the numerical errors of the flow solver. The ESGS model is based on the anisotropic minimum-dissipation (AMD) SGS model (Rozema *et al.* 2015) combined with a controller that iteratively adjusts the AMD eddy viscosity to match the DNS mean velocity profile. A Dirichlet non-slip boundary condition is applied at the walls and the correct wall-shear stress is enforced by augmenting the eddy viscosity at the walls such that $\nu_t|_w = (\partial\bar{u}/\partial y)|_w^{-1} \tau_w/\rho - \nu$, following Bae & Lozano-Durán (2021). For turbulent channel flows, the mean DNS quantities are obtained from the database by Jimenez and coworkers (Del Alamo *et al.* 2004; Hoyas & Jimenez 2006; Lozano-Durán & Jimenez 2014). Four cases with friction Reynolds numbers 550, 950, 2000 and 4200 are used. For the turbulent Poiseuille-Couette flows, our in-house code is used to generate DNS data. Two cases (labeled as PC-0 and PC-2) are considered, which correspond to separation and adverse pressure gradient, respectively. The Reynolds numbers based on the adverse pressure gradient are $Re_P = \sqrt{h^3 dP/dx}/\nu = 680$ and 340 , and the Reynolds number based on the top wall velocity is $Re_U = u_t h/\nu = 22,360$. The computational domain is $L_x \times L_y \times L_z = 4\pi h \times 2h \times 2\pi h$ for channel flows and $L_x \times L_y \times L_z = 2\pi h \times 2h \times \pi h$ for PC-0 and PC-2, where h is the channel half-height. The grid size for the WMLES cases with ESGS is $\Delta \approx 0.2h$.

2.3. Predictor and classifier

The architecture of the ANNs is a fully connected feedforward neural network with 6 hidden layers and 40 neurons per layer. The model comprises different ANNs. The first ANN is used to predict the eddy viscosity far from the wall, where viscous effects are negligible (i.e., outer layer ANN). To account for near-wall viscous effects, two ANNs are used to predict ν_t at the wall and at the first grid point off the wall. The input features to the outer layer ANN are $(I_1, \dots, I_6, \nu, \Delta)$. For inner layer ANNs, the input features are identical to the outer layer ANN in addition to $u_{||}$. The ANNs were trained using stochastic gradient descent by randomly dividing training data into two groups, the training set (80% of the data) and test set (20% of the data). For laminar flows, the eddy viscosity is set to zero.

The classification of the flow at a given point is done in two steps. First, the flow is classified as turbulent or laminar. If the flow is turbulent, it is further classified as zero-pressure-gradient wall turbulence (ZPG), adverse-pressure-gradient wall turbulence (APG), or separated turbulent flow. A Naive Bayes (NB) classifier is employed whose inputs are the nondimensionalized invariants (together with $u_{||}$ normalized with ν/Δ for the second classification). For the turbulent/laminar classifier, the invariants are normalized with ν and Δ , whereas for the second classification, $\sqrt{2S_{ij}S_{ij}}$ is used. The output of the classifier is a label that is fed to the predictor, as shown in Figure 1.

The classifier is trained with the same cases as the predictor in addition to synthetic data generated for laminar Poiseuille flow at $Re_\tau = [5 - 150]$. The classifier is applied to all grid points to discern between turbulent and laminar flow. The second classification is only applied to the points in contact with the wall. The classifier shows 100% accuracy in the first classification. For the turbulent classification, Figure 2(a) shows the confusion matrix. The numbers in the cells indicate the percentage of samples that are classified as a given class, showing that flows are predicted with $> 75\%$ accuracy.

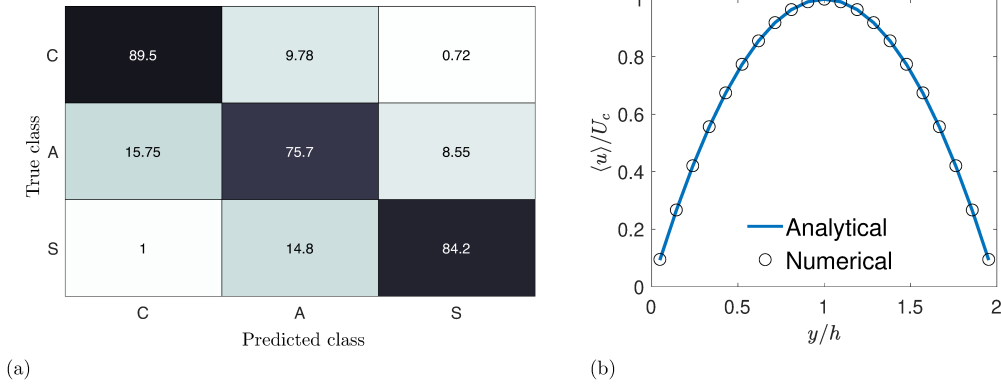


FIGURE 2. (a) Confusion matrix of the classifier for the first grid point off wall. C stands for ZPG flow, A for APG flow and S for separated flow. (b) Mean streamwise velocity profile for laminar channel flow (U_c is the centerline velocity).

3. Results

3.1. Laminar channel flow

The BFM is first tested in a laminar channel flow with fixed centerline velocity. The simulation is started from a random flow field and the data are collected after transients. As shown in Figure 2(b), the BFM produces the same solution as the analytical one by correctly classifying all the points as laminar flow. Regarding wall-shear stress, the analytical solution corresponds to a friction Reynolds number $Re_\tau = 19.64$, and the prediction of BFM is $Re_\tau = 19.62$.

3.2. Turbulent channel flow

The BFM is next tested in turbulent channel flows. Two grid sizes ($\Delta = 0.2h$ and $\Delta = 0.1h$) are considered to assess the generalizability of the model. The results of BFM are compared with the Dynamic Smagorinsky (DSM) and Vreman SGS models using the ODE-based equilibrium wall model (EQWM) by Larsson *et al.* (2016). The mean velocity profiles are shown in Figure 3, and Table 1 summarizes the friction Reynolds number predicted by WMLES. BFM exhibits the best performance in the coarse grid. The predictions of BFM deteriorate when the grid size is refined as shown in Figure 4; however, they are still comparable to those from traditional models. In this preliminary version of BFM, the model was trained only at one grid resolution. Better grid-convergence behavior is expected in future versions of BFM trained at various grid sizes.

3.3. Turbulent Poiseuille-Couette flow

Three cases are considered: PC0 (separation), PC1 (stronger APG) and PC2 (mild APG). The mean velocity profiles and wall-shear stress predictions are shown in Figure 5 and Table 1, respectively. As shown in Table 1, BFM gives the best wall-stress predictions for all cases. For PC0, BFM is capable of capturing separation better than other models. For PC2 and PC1, the improvement is marginal. As shown in Figure 5, BFM also outperforms or matches the accuracy of other models in terms of the prediction of the mean velocity profile except for PC1. The classifier was found to be responsible for hindering the overall performance in this case. Assuming a perfect classification for PC1, the results by BFM

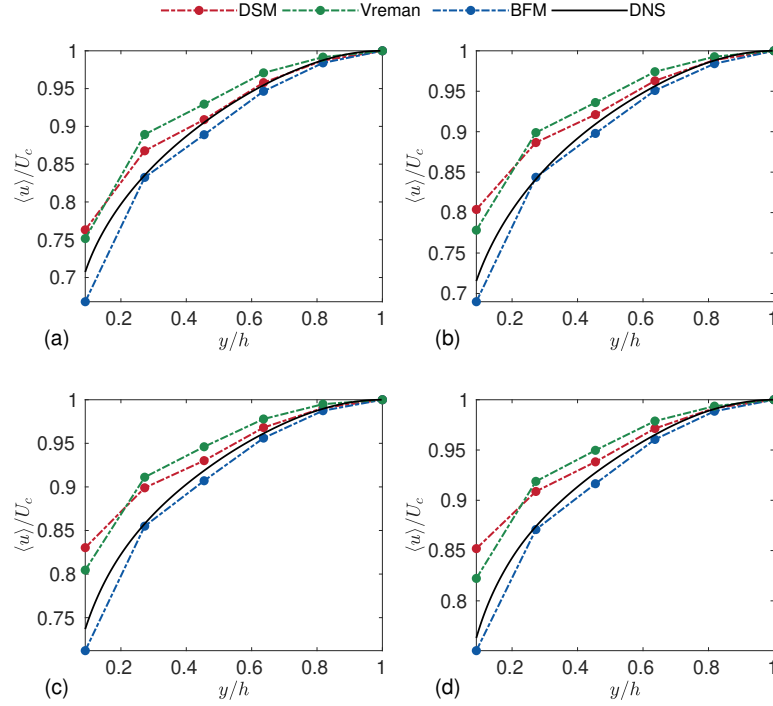


FIGURE 3. Mean streamwise velocity for turbulent channel flow using a coarse grid ($\Delta = 0.2h$). (a) $Re_\tau \approx 550$, (b) $Re_\tau \approx 950$, (c) $Re_\tau \approx 2000$ and (d) $Re_\tau \approx 4200$.

Case	Re_τ	DSM-EQWM	Vreman-EQWM	BFM	Trained	Re_P
550-C	547	587(7.3%)	578(5.7%)	540(1.3%)	✓	N/A
950-C	943	1034(9.7%)	1002(6.3%)	929(1.5%)	✓	N/A
2000-C	2003	2228(11.2%)	2157(7.7%)	1976(1.3%)	✓	N/A
4200-C	4179	4641(11.1%)	4474(7.1%)	4179(0.0%)	✓	N/A
550-M	547	552(0.9%)	545(0.4%)	537(1.8%)	✗	N/A
950-M	943	973(3.2%)	944(0.1%)	906(3.9%)	✗	N/A
2000-M	2003	2137(6.7%)	2050(2.3%)	1988(0.7%)	✗	N/A
4200-M	4179	4502(7.7%)	4286(2.6%)	4006(4.1%)	✗	N/A
PC0	7	76(1014%)	68(871%)	33(371%)	✓	680
PC1	194	164(15.5%)	169(12.9%)	172(11.3%)	✗	480
PC2	264	225(14.8%)	221(16.3%)	227(14.0%)	✓	340

TABLE 1. Friction Reynolds numbers predicted by different SGS and wall models. Re_τ are the benchmark values from DNS. The “Trained” column shows whether the case has been used for training. Cases ended with M were simulated with a finer grid ($\Delta = 0.1h$). Numbers in parentheses are the relative errors defined by $|(Re_{\tau, \text{pred}} - Re_\tau)/Re_\tau|$. Re_P is the Reynolds number defined by the adverse pressure gradient applied.

outperform other models, as shown in Figure 5. A more accurate classifier is anticipated to help the model achieve better mean profile and wall-shear stress predictions.

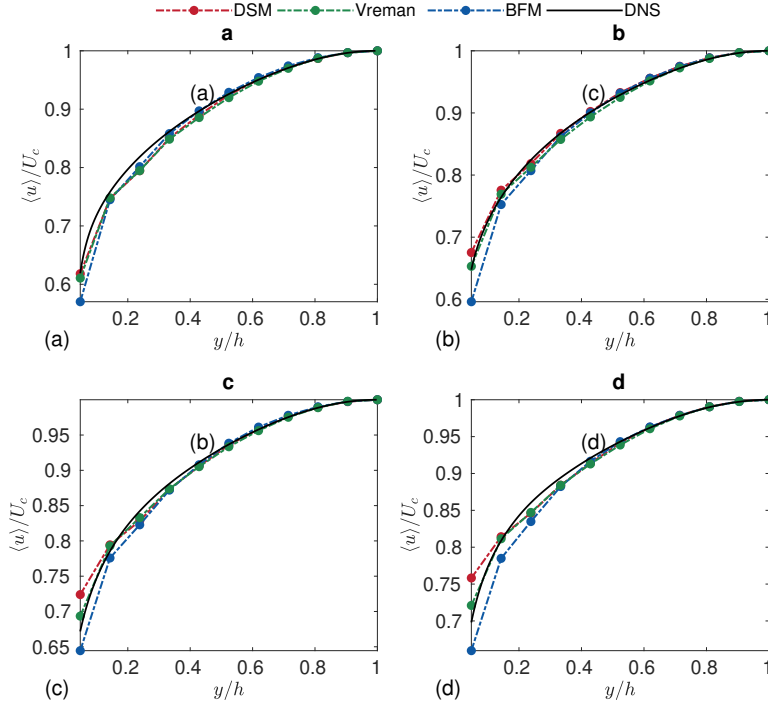


FIGURE 4. Mean streamwise velocity for turbulent channel flow using a medium grid ($\Delta = 0.1h$). (a) $Re_\tau \approx 550$, (b) $Re_\tau \approx 950$, (c) $Re_\tau \approx 2000$ and (d) $Re_\tau \approx 4200$.

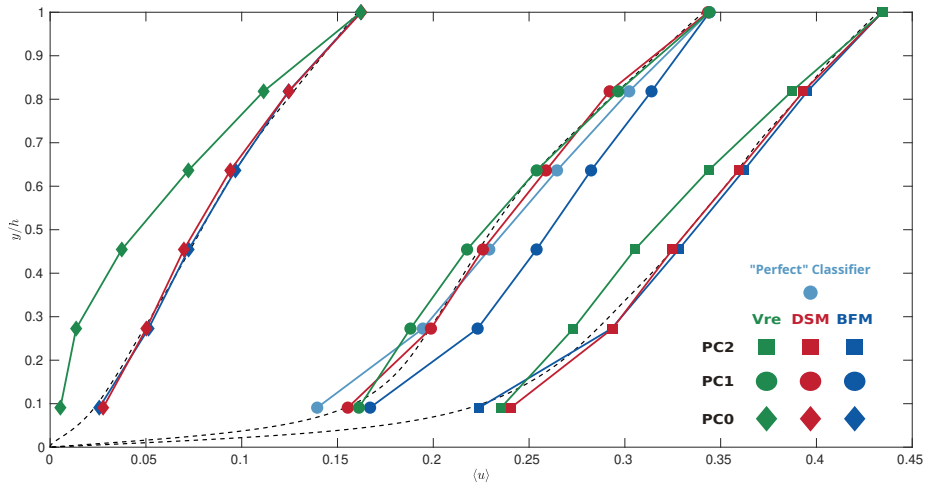


FIGURE 5. Mean streamwise velocity for Poiseuille-Couette flow. Three cases, PC0 (separation), PC1 (stronger APG) and PC2 (mild APG), are overlaid on the same plots.

3.4. CRM-HL

Finally, BFM is tested in the CRM-HL as representative of realistic aircraft in high-lift configuration (Lacy & Sclafani 2016). We focus on free air simulations. The reader is referred to Goc *et al.* (2022) for a detailed description of the physical and numerical setup.

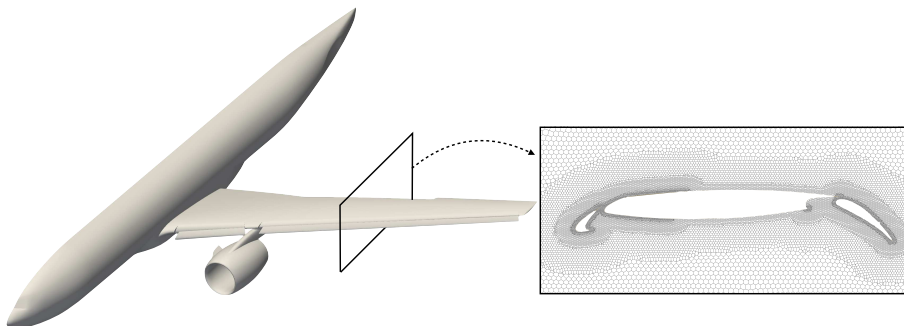


FIGURE 6. Geometry of the CRM-HL model and a cross-sectional view of the grid over the wing surface.

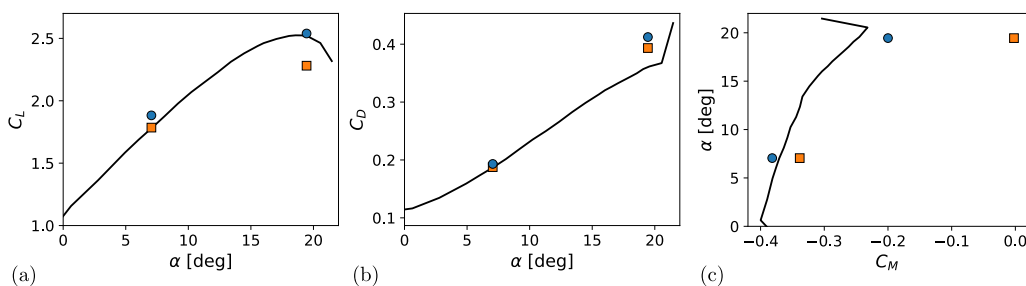


FIGURE 7. (a) Lift, (b) drag and (c) pitching moment coefficients for CRM-HL. The black lines denote experimental results, squares are for DSM-EQWM and circles are for BFM.

We perform simulations for two angles of attack, $\alpha = 7.05^\circ$ and 19.57° , and compare the lift, drag and pitching moment coefficients with experimental data and simulations from Goc *et al.* (2022) using DSM with EQWM (labeled as DSM-EQWM). The grid has 40 million elements and is the same as in Goc *et al.* (2022). A slice of the grid is depicted in Figure 6. The simulations are conducted in charLES with a version of BFM that assumes ZPG. Future versions of BFM will be retrained using WMLES data from charLES to guarantee accuracy in the classification and consistency with the numerical discretization.

Figure 7 displays the lift, drag and pitching moment coefficients. For $\alpha = 7.05^\circ$, DSM-EQWM correctly predicts C_L and C_D . However, further analysis has shown that this accurate prediction is coincidental and due to error cancellation when integrating the total forces. This is corroborated by the poor predictions of pitching moment by DSM-EQWM. However, BFM provides more consistent results. The case of $\alpha = 19.57^\circ$ corresponds to the angle of attack of maximum lift coefficient. DSM-EQWM underpredicts the C_L , whereas BFM accurately predicts C_L . The drag coefficient is overpredicted by both models, but the pitching moment computed using BFM is closer to the experimental values, suggesting that BFM provides a more accurate distribution of the forces over the wing. Inspection of the sectional pressure coefficient (Figure 8) indicates that BFM maintains the flow attached over a longer section of the wing compared to DSM-EQWM, which explains the enhanced performance of BFM.

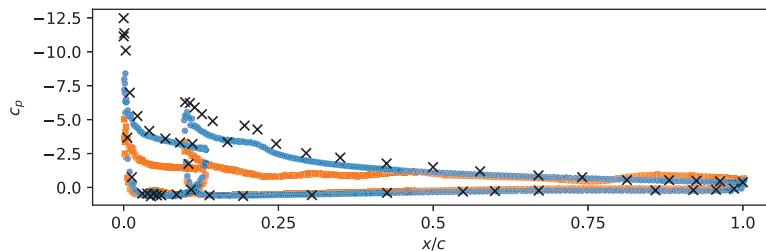


FIGURE 8. Pressure coefficient at the 82% spanwise section of the wing for $\alpha = 19.57^\circ$. Black \times represents experimental results, orange squares are for DSM-EQWM and blue circles are for BFM.

4. Conclusions

We have presented a unified SGS/wall model for large-eddy simulation by devising the flow as a collection of building blocks whose information enables the prediction of the SGS stress tensor. The model is referred to as the building-block flow model (BFM) and is grounded in the idea that truly revolutionary improvements in WMLES will encompass advancements in machine-learning-based modeling consistent with the numerics and grid generation.

The first version of BFM discussed here is constructed to predict wall-attached turbulence, adverse-pressure-gradient turbulence, separation and laminar flow. The model is trained using WMLES with an exact-for-the-mean SGS/wall model that guarantees consistency with the numerical schemes and the gridding strategy. The model is applicable to complex geometries and is implemented using artificial neural networks.

The BFM has been validated in canonical flows. These include laminar Poiseuille flow, turbulent channel flows, and turbulent Poiseuille-Couette flows mimicking adverse-pressure-gradient effects and separation. The performance of BFM in complex scenarios is evaluated in the NASA Common Research Model High-Lift (CRM-HL). We have shown that BFM outperforms traditional SGS/wall models in the canonical flows and the CRM-HL. The only exceptions are the coincidentally accurate predictions by the equilibrium wall model due to error cancellation. To the best of our knowledge, this is the first demonstration of a successful SGS/wall model implemented via artificial neural networks applicable to realistic aircraft configurations.

Acknowledgments

The authors acknowledge the MIT SuperCloud and Lincoln Laboratory Supercomputing Center for providing HPC resources that have contributed to the research results reported within this paper.

REFERENCES

- BAE, H. J. & KOUMOUTSAKOS, P. 2022 Scientific multi-agent reinforcement learning for wall-models of turbulent flows. *Nat. Commun.* **13**, 1443.
- BAE, H. J. & LOZANO-DURÁN, A. 2021 Effect of wall boundary conditions on a wall-modeled large-eddy simulation in a finite-difference framework. *Fluids* **6**, 112.
- CHOI, H. & MOIN, P. 2012 Grid-point requirements for large eddy simulation: Chapman estimates revisited. *Phys. Fluids* **24**, 011702.

- DEL ALAMO, J. C., JIMÉNEZ, J., ZANDONADE, P. & MOSER, R. D. 2004 Scaling of the energy spectra of turbulent channels. *J. Fluid Mech.* **500**, 135–144.
- GAMAHARA, M. & HATTORI, Y. 2017 Searching for turbulence models by artificial neural network. *Phys. Rev. Fluids* **2**, 054604.
- GOC, K., BOSE, S. T. & MOIN, P. 2022 Large eddy simulation of the NASA high-lift common research model. In *AIAA SCITECH 2022 Forum*, p. 1556.
- GOC, K. A., LEHMKUHL, O., PARK, G. I., BOSE, S. T. & MOIN, P. 2021 Large eddy simulation of aircraft at affordable cost: a milestone in computational fluid dynamics. *Flow* **1**, E14.
- HOYAS, S. & JIMÉNEZ, J. 2006 Scaling of the velocity fluctuations in turbulent channels up to $Re_\tau = 2003$. *Phys. Fluids* **18** (1), 011702.
- HUANG, X. L., YANG, X. I. & KUNZ, R. F. 2019 Wall-modeled large-eddy simulations of spanwise rotating turbulent channels—Comparing a physics-based approach and a data-based approach. *Phys. Fluids* **31**, 125105.
- LACY, D. S. & SCLAFANI, A. J. 2016 Development of the high lift common research model (hl-crm): A representative high lift configuration for transonic transports. In *54th AIAA Aerospace Sciences Meeting*, p. 308.
- LARSSON, J., KAWAI, S., BODART, J. & BERMEJO-MORENO, I. 2016 Large eddy simulation with modeled wall-stress: recent progress and future directions. *Mech. Eng. Rev.* **3**, 15–00418.
- LOZANO-DURÁN, A. & BAE, H. J. 2020 Self-critical machine-learning wall-modeled LES for external aerodynamics. *Annual Research Briefs*, Center for Turbulence Research, Stanford University, pp. 197–210.
- LOZANO-DURÁN, A., BOSE, S. T. & MOIN, P. 2022 Performance of wall-modeled LES with boundary-layer-conforming grids for external aerodynamics. *AIAA J.* **60**, 747–766.
- LOZANO-DURÁN, A. & JIMÉNEZ, J. 2014 Effect of the computational domain on direct simulations of turbulent channels up to $Re_\tau = 4200$. *Phys. Fluids* **26**, 011702.
- LUND, T. S. & NOVIKOV, E. 1993 Parameterization of subgrid-scale stress by the velocity gradient tensor. *Annual Research Briefs*, Center for Turbulence Research, Stanford University, pp. 27–43.
- ROZEMA, W., BAE, H. J., MOIN, P. & VERSTAPPEN, R. 2015 Minimum-dissipation models for large-eddy simulation. *Phys. Fluids* **27**, 085107.
- SMITS, A. J. & MARUSIC, I. 2013 Wall-bounded turbulence. *Phys. Today* **66**, 25–30.
- XIE, C., WANG, J., LI, H., WAN, M. & CHEN, S. 2019 Artificial neural network mixed model for large eddy simulation of compressible isotropic turbulence. *Phys. Fluids* **31**, 085112.
- YANG, X. I. A. & GRIFFIN, K. P. 2021 Grid-point and time-step requirements for direct numerical simulation and large-eddy simulation. *Phys. Fluids* **33**, 015108.
- YANG, X. I. A., ZAFAR, S., WANG, J.-X. & XIAO, H. 2019 Predictive large-eddy-simulation wall modeling via physics-informed neural networks. *Phys. Rev. Fluids* **4**, 034602.
- ZANGENEH, R. 2021 Data-driven model for improving wall-modeled large-eddy simulation of supersonic turbulent flows with separation. *Phys. Fluids* **33**, 126103.
- ZHOU, Z., HE, G. & YANG, X. 2021 Wall model based on neural networks for LES of turbulent flows over periodic hills. *Phys. Rev. Fluids* **6**, 054610.